Lasers in Manufacturing Conference 2019

Modeling and simulation of laser micro welding

Christoph Schöler[a*], Markus Nießen[b], Marc Hummel[c], Alexander Olowinsky[b], Arnold Gillner[b,c], Wolfgang Schulz[a,b]

[a]*RWTH Aachen University, Nonlinear Dynamics of Laser Processing NLD, Steinbachstr. 15, 52074 Aachen, Germany*
[b]*Fraunhofer Institute for Laser Technology ILT, Steinbachstr. 15, 52074 Aachen, Germany*
[c]*RWTH Aachen University, Chair for Laser Technology LLT, Steinbachstr. 15, 52074 Aachen, Germany*

Abstract

Laser welding using fiber lasers of high power and quality facilitate the joining of highly conductive materials while attaining high aspect ratio welds at spot sizes in the micrometer range. Industrial applications are laser bonding of copper contacts in power electronics and battery modules. An important quality feature is a defined weld seam geometry which is determined by the physical transport phenomena during the process. This contribution targets the development of a model that serves as a basis for experimental control strategies. Reasonable assumptions for reducing the model's complexity are made by exploiting the characteristic length and time scales of the process. Laser absorption at the metal surface and heat conduction in the material are considered as the dominant phenomena to define the shape of the keyhole. Simulations are subjected to parameter variations and validated by experimental reference data.

Keywords: laser micro welding; weld seam geometry; modeling; simulation, 515 nm; green laser

1. Introduction

In the fabrication of components for electro mobility, lasers with high power and small spot sizes are used to join single battery cells to battery packs by contacting them with copper connectors (Schmidt, 2015). In order to provide bonds with high mechanical as well as electrical load-bearing capacities, for instance during fast charging when high currents pass through the bond cross-section, a continuous weld seam is required. Even more crucial however is to avoid the penetration of heat or even laser light through the electrodes as it causes damage to the sealing and might lead to ignition of the internal chemicals thus deteriorating the

* Corresponding author. Tel.: +49-241-8906-8307; fax: +49-241-8906-121.
E-mail address: christoph.schoeler@nld.rwth-aachen.de.

battery pack in which the cell is embedded. To satisfy these demands a stable welding process which is distinguished by low porosity and a controlled weld depth has to be guaranteed. It is the major task of process development to establish such a welding process and to identify parameter regimes that ensure a high reducibility of bonds and low waste of electronic components. The motivation for modeling and simulation is to support this development by contributing to the understanding of the process mechanisms and to avoid extensive and costly experimental parameter studies by predictive calculations.

1.1. Laser micro welding of copper

Laser micro welding of copper is a challenging task on its own. The high electrical conductivity of copper makes it a suitable choice from the perspective of electrical efficiency but at the same time brings challenges for weldability owing to its high thermal conductivity and low absorptivity in the near-infrared. Laser beam sources in the near-infrared range from 1030-1070 nm have been established as state of the art in laser micro welding of copper materials (Auwal et al., 2018). Despite major improvements through process development melt ejections, pore formation, and process instabilities remain unresolved problems (Hess, 2012, Schmitt, 2012, Haeusler et al., 2017). As the absorptivity of copper in the near-infrared region is below five percent and raises by a factor of ten throughout the visible region green and blue laser beam sources have become more interesting for welding applications (Engler et al., 2011, Hess et al., 2011, Zediker et al., 2018). Reproducible laser welds on copper foils using a frequency-doubled green laser were reported by Bono et al., 2013, and Pricking et al., 2016 demonstrated a high reproducibility of heat conduction laser welds regarding seam width and depth using a newly developed green frequency doubled pulsed disk laser with pulse peak powers ranging up to 8 kW and a beam parameter product below 5 mm mrad.

1.2. Weld depth specifications

With respect to lack of fusion in the lap joint geometry and to potential damaging or destruction of the battery cells the weld seam depth is considered to be the main criterion for high quality bonds. Target values of the weld depth depend on the type of the battery cell and the thickness of the conductor plate. A prominent battery cell design for electro mobility are round cells which provide the highest gravimetric and volumetric energy density compared to other available types (Thielmann et al., 2017). The cross-section of a 18650-type battery cell and the weld configuration are depicted in figure 1. It shows that the material thicknesses of the negative and positive poles on which the bonds are performed are in the order of 270 µm and 500 µm, respectively. Taking into account the typical thickness of a copper connector leads to weld depths in the ranges of 300-400 µm and 500-700 µm. These target values will dictate the range of the process parameters, namely feed rate, focal diameter, and laser power.

1.3. Objectives and methodology

The scope of the present work is to investigate steady-state keyhole shapes for bead-on-plate micro welds on copper with a green laser by modeling and simulation. For this purpose a simplified model that has been developed for laser deep penetration welding and facilitates an efficient computation of the keyhole shape as a function of process parameters is employed. We expect that the knowledge of the keyhole depth, although not reproducing the weld seam depth exactly, will already yield key information on process characteristics that influence the weld depth as well as the process stability. This approach is chosen to provide an enhanced understanding of the formation of the welding keyhole and thus to support the development of control strategies for the experiment, and to enable fast predictions of the process result.

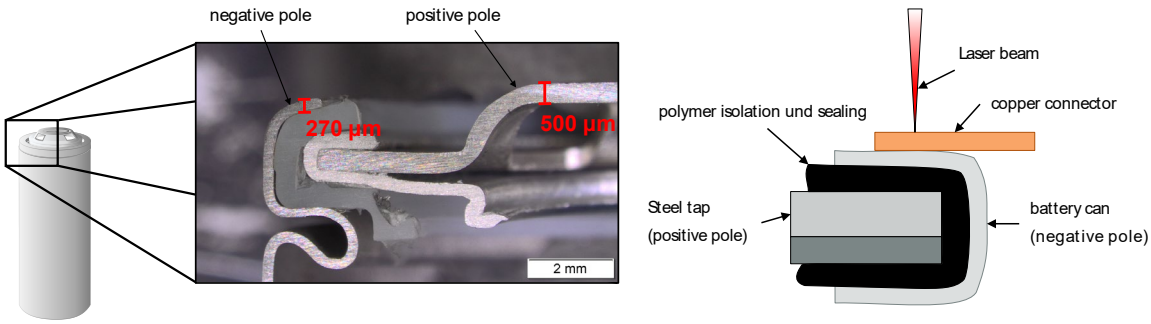

Fig. 1. (a) Photograph of a cross-section of a 18650-type battery can with indication of material thicknesses at the positive and negative poles. (b) Schematic view of the weld configuration of a copper bond on the negative pole of the battery cell.

In order to obtain the keyhole shape a system of continuum-physical balancing equations is formulated and solved after discretizing the calculation domain into a set of two-dimensional layers. The equations account for the conservation of mass, momentum, and energy across the liquid-gas interface at the keyhole front. The transport problem in the liquid and solid phases is not solved numerically but regarded by taking analytic solutions that approximate the steady-state conditions. The intensity distribution of the absorbed laser light on the keyhole surface is calculated by a ray tracing algorithm in order to account for the contributions of multiple reflections inside the keyhole. The depths of the resulting keyholes are compared to experimental measurements of the seam depth for welds conducted in Cu-ETP for a variety of process parameters.

2. Keyhole model

The keyhole model is based on a fundamental geometric property of weld seams in laser deep penetration welding. The seams are characterized by high aspect ratios, that is, the ratio of seam depth to seam width. In order to obtain these ratios the laser light has to penetrate deep into the material through a narrow keyhole which leads to a steep keyhole surface. Taking into account a thin melt film in front of the laser beam a spatial boundary layer in the direction lateral to the laser beam axis and normal to the keyhole front arises. This knowledge motivates a separation of the spatial dimensions as it was discussed thoroughly by Schulz et al., 2009. We therefore treat the transport phenomena decoupled from the axial spatial dimension in two-dimensional lateral layers and introduce the axial coupling through Fresnel absorption and light propagation.

2.1. Layer model parameters

Modeling the physical transport phenomena in deep penetration laser welding is a cumbersome task as it involves the description of multiple phases that are governed by the interactions at the free phase boundaries (Dowden, 2009). The loci of the phase boundaries are generally determined by the local conditions at the interfaces. For the purpose of further model reduction we assume that the geometric shape of the keyhole surface in its steady-state in each layer approximately takes the form of a circle with *layer radius* R. Moreover we neglect variations of the surface temperature along the layer surface which leads to the constant *layer surface temperature* T_s. Lastly we introduce the relative position of the keyhole front with respect to the laser beam axis as *layer front position* A. These three layer model parameters are

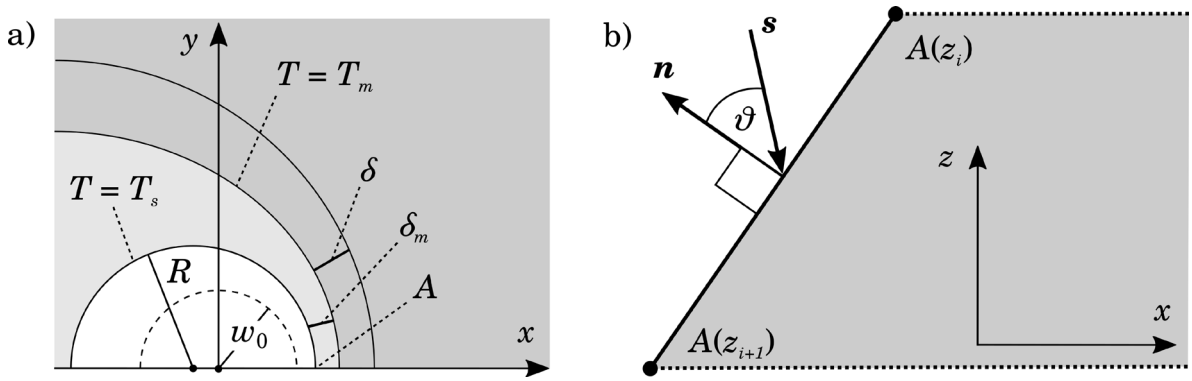

Fig. 2. (a) Sketch of the layer model with parameters layer radius R, layer front position A, and layer surface temperature T_s. The white area indicates the layer cross-section of the keyhole. Further quantities: laser beam radius w_0, melt film thickness δ_m, melt line $T = T_m$, and penetration depth of heat in the solid δ. (b) Incidence of the laser beam at the vertically inclined keyhole front with surface normal vector $\boldsymbol{n}$, Poynting vector $\boldsymbol{s}$, and angle of incidence ϑ.

illustrated in figure 2. Their values will be determined by conditional equations which are presented in the subsequent sections.

2.2. Balancing equations

The transition from the liquid to the gaseous phase is described by the conservation of mass, momentum, and energy flux densities across the evaporating surface in consideration of the discontinuous changes of the physical state properties density ρ, temperature T, (normal) velocity component relative to the interface u, and pressure P. Following the work of Aden et al., 1992, from the steady-state conservation equations a set of conditional equations is derived for local evaluation at the layer front position of each layer:

$$\rho_g u_g = \rho_l u_l \tag{1}$$

$$\rho_g u_g^2 + P_g = P_l + \sigma/R \tag{2}$$

$$\rho_g u_g \Delta = q_a - q_l \tag{3}$$

where the subscript l and g denote the properties in the liquid and gaseous phase, respectively. Furthermore, q_a denotes the laser intensity being absorbed at the keyhole surface, q_l the energy flux density entering the liquid phase, Δ the specific latent heat of vaporization, and σ the surface tension. It shall be noted that the liquid velocity u_l is neglected in all terms except for the mass conservation equation (1) and that we do not account for corrections due to the temperature jump as we assume the case of small flow Mach numbers at the exit of the Knudsen layer. The last term in equation (2) is the Laplace pressure for a cylindrical surface.

The final conditional equation for the layer model is obtained from a global power balance which is obtained by integrating equation (3) over the layer surface. We assume that the vapor flow is nearly completely confined in the layer plane and the energy which is spent to evaporate particles from the front side of the keyhole surface is fed back to the material at its back side upon condensation. Hence the left-hand side of equation (3) equates to zero after integration and the global power balance is given by

$$\oint (q_a - q_l)\, d\Omega = 0. \tag{4}$$

2.3. Liquid and gaseous state approximations

The mass efflux $\rho_g u_g$ and the dynamic gas pressure $\rho_g u_g^2$ are established from a Hertz-Knudsen evaporation model that relates them to the gas pressure and the surface temperature, assuming that the emitted particles leave the surface at saturated conditions and that $T_g \approx T_s$ (c.f. Schrage, 1953):

$$\rho_g u_g = 1/\sqrt{2\pi R_m T_s} \cdot \left(P_s(T_s) - P_g\right) \tag{5}$$

where $R_m = k_B/m$ denotes the specific gas constant and P_s the saturation pressure which is evaluated according to the Clausius-Clapeyron equation for ideal gases (e.g. see Callen, 1985). For further simplification it is assumed that the gas pressure P_g is close to the pressure of the surrounding air and is chosen as constant. An estimation of the liquid pressure from the typical depth of the melt pool and a stagnation point at the keyhole front leads to an excess pressure in the order of millibar compared to the ambient pressure. Comparing orders of magnitude in equation (2) then leaves the balancing of capillary forces by recoil forces.

The heat flux into the liquid q_l is obtained from the two-dimensional heat conduction solution for a homogeneously advected material through a circular interface which is at temperature T_s (Schulz et al., 1993). This is a known limitation of the current model as it does not represent the flow situation around the keyhole correctly and will be improved in the future. An analysis in boundary fitted coordinates (Kostrykin et al., 2004) shows that the temperature distribution when approximated by the monopole term of the infinite sum of Bessel functions takes a simple form and the heat flux at the interface under the azimuth φ is given by

$$q_l(\varphi) = -\lambda \cdot \partial_r T(r,\varphi)|_{r=A} = \lambda(T_s - T_0) Pe' [\cos\varphi + K_1(Pe'R)/K_0(Pe'R)], \quad Pe' = v_0/2\kappa \tag{6}$$

where λ is the thermal conductivity, κ the thermal diffusivity, v_0 the feed rate, and T_0 the ambient temperature. The functions K_0 and K_1 are the modified Bessel function of the second kind of respective orders 0 and 1. The result equals the heat flux formula for a moving line source used by Kaplan, 1994. In order to account for the (specific) latent heat of fusion h_m upon melting and solidification the heat flux from equation (6) is modified by addition of the term $\rho_l h_m v_0$ before substituting it into equation (3).

2.4. Axial coupling

The axial coupling between the layers is established by accounting for the dependence of the absorbed laser intensity on the incidence angle ϑ which is defined as the angle between surface normal vector $\boldsymbol{n}$ and Poynting vector $\boldsymbol{s}$ (see figure 2). The local normal vectors are obtained from a discretization of the layer circles by the azimuthal angle and the connection of the circular sections between adjacent layers. Including the contributions of multiple reflections denoted by MR the local value of the absorbed intensity is given by

$$q_a = \mu\, A(\mu)\, I_L + MR, \quad \mu = \cos\vartheta \tag{7}$$

where I_L is the directly impinging intensity of the laser beam and A is the absorptance of the material due to the Fresnel equations. Its dependence on μ for circular polarized light is taken as

$$A(\mu) = 2\epsilon\mu\, [1/(\epsilon^2 + 2\epsilon\mu + 2\mu^2) + 1/(2 + 2\epsilon\mu + \epsilon^2\mu^2)] \tag{8}$$

where ϵ is a material parameter that depends on the wavelength of the laser light (c.f. Schulz et al., 1987).

The calculation procedure for the three-dimensional keyhole shape starts from top of the workpiece and continues downwards by iteratively adding new layers. The normal vectors of the initial layer are prescribed and the parameters of each layer are determined by a root finding algorithm in order to fulfill the conditional equations (2), (3), and (4). Raytracing is performed in every iteration to obtain the term MR for equation (7). Once a layer has been calculated it is added to the set of keyhole layers and will not be changed anymore. The calculation is terminated when the layer radius falls below a prescribed minimum value.

3. Results and discussion

3.1. Experimental setup and simulation parameters

For the experimental setup a Trumpf TruDisk Pulse 421 frequency-doubled disc laser beam source with a wavelength of 515 nm is used. The laser outputs an average power of 400 W and allows for pulse durations between 0.3 and 50 ms. The laser beam is guided through a fiber with a diameter of 100 µm and focused by a F-theta lens. The beam profile about the focal plane is measured with a micro spot monitor and yields focal diameter, beam quality factor, and the intensity distribution near the beam waist. Due to the pulsed operating mode laser seam welding is conducted only for the length of one pulse to generate a quasi-continuous weld as it was developed by Kramer et al., 2002. Since power measurements in the working plane are not available the nominal peak powers from the operating software of the laser are taken for identification of the parameter sets. To account for losses in the beam path the peak powers are multiplied by a loss factor that is calibrated once for each focusing optic by an initial simulation run. The focal position of the laser beam is always placed on top of the material. The resulting laser beam parameters are summarized in table 1.

Table 1. Laser beam parameters.

Focusing optic	Power loss factor [1]	Focal diameter [µm]	M^2 beam quality factor [1]	Beam profile
F80	0.98	242	24.5	Gaussian
F163	0.86	326	22.6	Super-Gaussian, order 2

The process parameters are chosen to meet the range specifications for the weld seam (c.f. section 1.2). They are listed in table 2 and hereafter will be referred to via their IDs. The material parameters are listed in table 3 and are taken as constant as prescribed by the model assumptions. The thermo-physical properties were obtained from Deutsches Kupferinstitut, 2005, Lossin, 2000, and Zhang et al., 2011. The surface tension was extrapolated to the boiling point from data measured by Brillo and Egry, 2005. The absorptance is calculated from values of the optical constants measured by Johnson and Christy, 1972 on vacuum-evaporated thin films at room temperature. The ambient temperature is set to 20 °C.

Table 2. Process parameters.

Parameter \ ID	#1	#2	#3	#4	#5	#6
Focusing optic	F80	F80	F163	F163	F163	F163
Peak power [W]	850	700	1400	1700	1600	1500
Feed rate [mm s^{-1}]	80	20	100	80	60	40

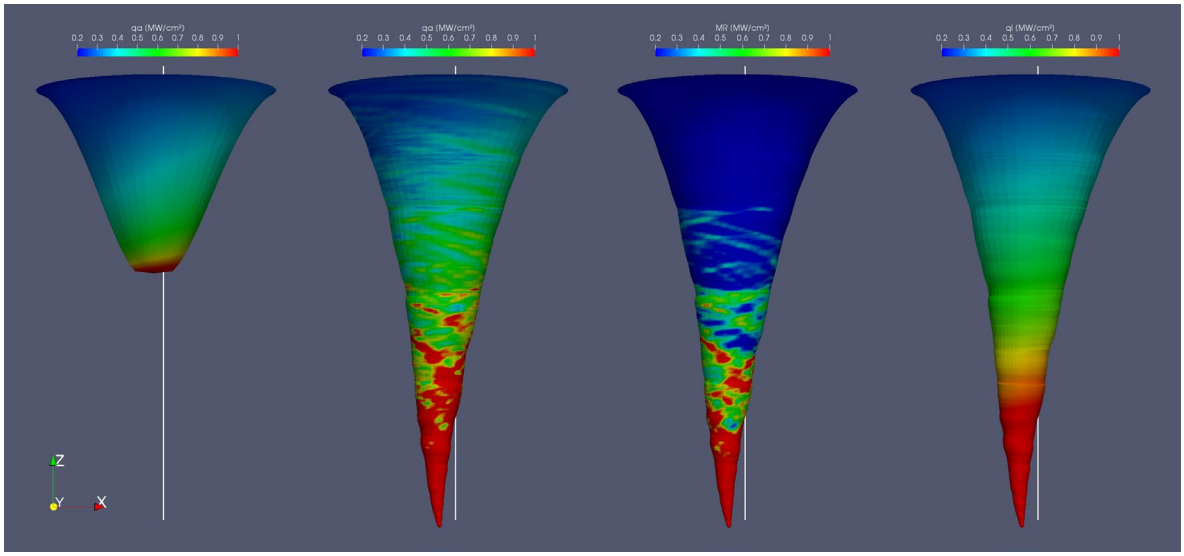

Fig. 3. Example of a calculated welding keyhole. From left to right: keyhole shape and total absorbed intensity without MR contributions, total absorbed intensity, share in the total absorbed intensity by MR, heat flux into the material after equation (6). The vertical white lines indicate the laser beam axis.

Table 3. Material parameters for Cu-ETP.

Density in condensed state [g cm^{-3}]	Thermal conductivity [W m^{-1} K^{-1}]	Thermal diffusivity [cm^2 s^{-1}]	Specific heat of fusion [kJ g^{-1}]	Specific heat of vaporization [kJ g^{-1}]	Specific gas constant [J g^{-1} K^{-1}]	Surface tension [N m^{-1}]	Evaporation temperature [K]	Absorptance at normal incidence [1]
8.930	394	1.1430	0.2093	4.7997	0.1308	0.95	2868.15	0.4122

3.2. Keyhole simulations

The result of an exemplarily calculated keyhole is depicted in figure 3. The left plot shows the keyhole shape and the distribution of the absorbed intensity on its surface for a reference calculation in which the raytracing module was disabled. It illustrates the significance of the absorption of reflected light for the formation of the weld seam also in the case for the highly absorptive green laser light. The plots to the right show the distributions of three quantities on the keyhole surface that was calculated with the same set of process parameters including the absorption contributions MR from reflected light rays. The rightmost plot illustrates how heat flux losses increase as a function of the layer radius according to equation (6). Comparing the distributions of the total absorbed intensity q_a and the MR contributions the keyhole can be subdivided into two regions. The upper part of the keyhole is mostly governed by light that directly impinges on the surface from the incoming laser beam. Through reflections off the metallic surface light intensity is transported into the deeper regions of the keyhole and there forms its shape according to the history of the ray paths. The ray paths are the consequence of the relative orientations between Poynting vectors and surface normals.

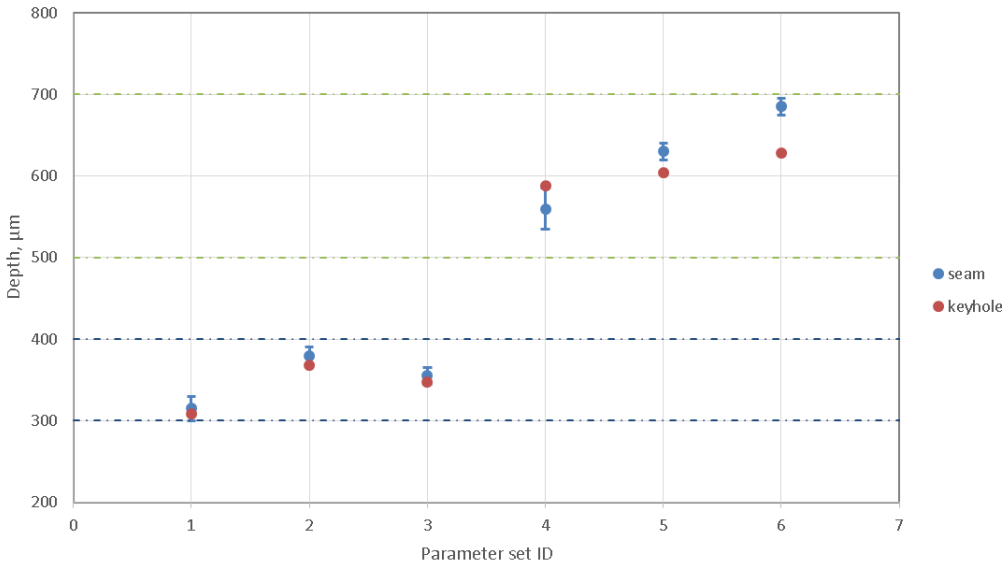

Fig. 4. Comparison of calculated keyhole depths with measured values of the seam depth for parameter sets listed in table 2. The horizontal lines mark the seam depth range specifications for bonds on copper connectors.

In the deeper layers the distribution of the MR-intensity is strongly inhomogeneous as rays strike the surface under all azimuthal angles. When an excessive amount of intensity is encountered across the whole surface of a layer bulges begin to form. These give rise to convex surfaces which again lead to focusing of light in the layers underneath. At the bottom part the keyhole becomes narrow and tends to bend forward against the feeding direction in order to adapt to the light that channels in the needle-like cavity. The steady-state shape obtained with our approximate model therefore indicates an inherent instability of the keyhole in the dynamic case: the intensity hot spots due to multiple reflections indicate where local increases in evaporation rates may set in and trigger strong driving forces on the surface which lead to an instability of the process.

3.3. Weld depth comparison

The experimentally measured weld seam depths and the simulated keyhole depths are shown in figure 4. For every the parameter set from table 2 the experiment was conducted three times for statistical purpose. The seam depth is measured from longitudinal sections of the weld seam to ensure steady-state conditions. When comparing the keyhole depth with the seam depth to it must be noted that a considerable melt film can be present below the keyhole bottom because of the high thermal conductivity of copper and the low weld speeds. Furthermore, there can be uncertainties in preparing the longitudinal sections and taking the seam depth values. Taking this into account a good agreement between simulation and experiment could be obtained for all investigated parameter sets. The calculated values of the keyhole depth show the same trends under variations in feed rate and laser power. From these results we conclude that our model is suitable to predict the welding depth even though it does not account for the exact three-dimensional keyhole shape. Its applicability range has to be investigated in the future by a broader parameter study.

4. Conclusion

A welding model which calculates the three-dimensional keyhole shape has been presented. The model complexity has been strongly reduced by exploiting the characteristic length and time scales of the process. Direct laser absorption and multiple reflections were taken into account to balance heat conduction losses. A global power balance is fulfilled for the assumption of a circular keyhole shape in every horizontal plane. It was found that the contribution of multiple reflections to the absorbed laser power dominantly defines the vertical shape of the keyhole and thus the weld depth. Calculated keyhole depths agree well with experimental measurements of the weld seam. The next steps will be to take into account the melt flow around the keyhole and to lower the restriction that the shape in each layer takes the form of a circle. Extensions for the calculation of three-dimensional temperature distributions are planned and comparisons with three-dimensional weld seam measurements will validate the suitability of the model for predictive calculations of equivalent heat sources for the numerical evaluation of weld stresses and distortion.

Acknowledgements

The presented investigations were carried out within the framework of the Collaborative Research Centre SFB1120 “Bauteilpräzision durch Beherrschung von Schmelze und Erstarrung in Produktionsprozessen” and funded by the Deutsche Forschungsgemeinschaft e.V. (DFG). The sponsorship and support is gratefully acknowledged.

References

Aden, M., Beyer, E., Herziger, G., Kunze, H., 1992. Laser-induced vaporization of a metal surface, Journal of Physics D: Applied Physics 1, p. 57.

Auwal, S., Ramesh, S., Yusof, F., Manladan, S., 2018. A review on laser beam welding of copper alloys, The International Journal of Advanced Manufacturing Technology 1-4, p. 475.

Bono, P. de, Metsios, I., Blackburn, J., Hilton, P. Laser processing of thin copper and aluminium thin sheets with green (532nm) and infrared (1064nm) pulsed laser beam sources, in "*International Congress on Applications of Lasers & Electro-Optics*". Laser Institute of America, p. 520.

Brillo, J., Egry, I., 2005. Surface tension of nickel, copper, iron and their binary alloys, Journal of Materials Science 9-10, p. 2213.

Callen, H., 1985. Thermodynamics and an introduction to thermostatistics, 2. ed. Wiley, New York, NY.

Deutsches Kupferinstitut, 2005. Werkstoff-Datenblatt Cu-ETP - CW004A. https://www.kupferinstitut.de.

Dowden, J., 2009. The Theory of Laser Materials Processing. Springer Netherlands, Dordrecht.

Engler, S., Ramsayer, R., Poprawe, R., 2011. Process Studies on Laser Welding of Copper with Brilliant Green and Infrared Lasers, Physics Procedia, p. 339.

Haeusler, A., Schürmann, A., Schöler, C., Olowinsky, A., Gillner, A., Poprawe, R., 2017. Quality improvement of copper welds by laser microwelding with the usage of spatial power modulation, Journal of Laser Applications 2, p. 22422.

Hess, A., 2012. Vorteile und Herausforderungen beim Laserstrahlschweißen mit Strahlquellen höchster Fokussierbarkeit, Dissertation. Universität Stuttgart, Stuttgart.

Hess, A., Schuster, R., Heider, A., Weber, R., Graf, T., 2011. Continuous Wave Laser Welding of Copper with Combined Beams at Wavelengths of 1030nm and of 515nm, Physics Procedia, p. 88.

Johnson, P., Christy, R., 1972. Optical Constants of the Noble Metals, Physical Review B 12, p. 4370.

Kaplan, A., 1994. A model of deep penetration laser welding based on calculation of the keyhole profile, Journal of Physics D: Applied Physics 9, p. 1805.

Kostrykin, V., Schulz, W., Nießen, M., Michel, J., 2004. Short-Time Dynamics in Laser Material Processing, in "*Nonlinear Dynamics of Production Systems*", G. Radons, R. Neugebauer, Editor. Wiley-VCH Verlag GmbH & Co. KGaA, Weinheim, FRG, p. 443.

Kramer, T., Olowinsky, A., Durand, F., 2002. SHADOW: a new welding technique, in "*Photon Processing in Microelectronics and Photonics*", K. Sugioka, M. C. Gower, J.R. F. Haglund, A. Pique, F. Traeger, J. J. Dubowski, W. Hoving, Editor. SPIE, p. 545.

Lossin, A., 2000. Copper, in "*Ullmann's Encyclopedia of Industrial Chemistry*". Wiley-VCH Verlag GmbH & Co. KGaA, Weinheim, Germany, p. 15.

Pricking, S., Huber, R., Klausmann, K., Kaiser, E., Stolzenburg, C., Killi, A., 2016. High-power CW and long-pulse lasers in the green wavelength regime for copper welding, in "*High-Power Laser Materials Processing: Lasers, Beam Delivery, Diagnostics, and Applications V*", F. Dorsch, S. Kaierle, Editor. SPIE, p. 97410G.

Schmidt, P., 2015. Laserstrahlschweißen elektrischer Kontakte von Lithium-Ionen-Batterien in Elektro- und Hybridfahrzeugen, Dissertation. Technische Universität München, München.

Schmitt, F., 2012. Laserstrahl-Mikroschweißen mit Strahlquellen hoher Brillanz und örtlicher Leistungsmodulation, Dissertation. RWTH Aachen, Aachen.

Schrage, R., 1953. A theoretical study of interphase mass transfer. Columbia Univ. Press, New York.

Schulz, W., Becker, D., Franke, J., Kemmerling, R., Herziger, G., 1993. Heat conduction losses in laser cutting of metals, Journal of Physics D: Applied Physics 9, p. 1357.

Schulz, W., Nießen, M., Eppelt, U., Kowalick, K., 2009. Simulation of Laser Cutting, in "*The Theory of Laser Materials Processing*", J. Dowden, Editor. Springer Netherlands, Dordrecht, p. 21.

Schulz, W., Simon, G., Urbassek, H., Decker, I., 1987. On laser fusion cutting of metals, Journal of Physics D: Applied Physics 4, p. 481.

Thielmann, A., Neef, C., Hettesheimer, T., Döscher, H., Wietschel, M., Tübke, J., Dezember 2017. Energiespeicher-Roadmap (Update 2017) - Hochenergie-Batterien 2030+ und Perspektiven zukünftiger Batterietechnologien. Fraunhofer-Institut für System- und Innovationsforschung ISI, Karlsruhe.

Zediker, M., Silva Sa, M., Finuf, M., Fritz, R., Tucker, J., Pelaprat, J., 2018. Blue laser diode (450 nm) system for welding copper, in "*Proc. SPIE 10514, High-Power Diode Laser Technology XVI*", M. S. Zediker, Editor. SPIE, San Francisco, p. 1051407.

Zhang, Y., Evans, J., Yang, S., 2011. Corrected Values for Boiling Points and Enthalpies of Vaporization of Elements in Handbooks, Journal of Chemical & Engineering Data 2, p. 328.